Fluctuations at the onset of discontinuous shear thickening in a suspension

Omer Sedes, Abhinendra Singh, and Jeffrey F. Morris

Citation: Journal of Rheology **64**, 309 (2020); doi: 10.1122/1.5131740
View online: https://doi.org/10.1122/1.5131740
View Table of Contents: https://sor.scitation.org/toc/jor/64/2
Published by the The Society of Rheology

Fluctuations at the onset of discontinuous shear thickening in a suspension

Omer Sedes,[1] Abhinendra Singh,[2] and Jeffrey F. Morris[1,a)]

[1]*Benjamin Levich Institute and Department of Chemical Engineering, CUNY City College of New York, New York, New York 10031*
[2]*James Franck Institute and Pritzker School of Molecular Engineering, University of Chicago, Illinois 60637*

(Received 15 October 2019; final revision received 11 January 2020; published 4 March 2020)

Abstract

Discontinuous shear thickening (DST) in concentrated suspensions is accompanied by pronounced fluctuations in the measured viscosity under a fixed shear rate. In this work, the suspension flow is simulated by a discrete-particle method, in which a repulsive force of magnitude F_R between neighboring particles maintains viscous liquid lubricating films for stress $\sigma < \sigma_0 \sim F_R a^{-2}$ with a being the particle radius; when the films rupture, frictional contacts form. The suspension rheology displays continuous or discontinuous shear thickening for ϕ below or above ϕ_c, respectively. The apparent critical point $(\phi_c, \dot{\gamma}_c)$ on the viscosity curve dividing these behaviors is identified as the point at which $\partial\langle\sigma\rangle/\partial\dot{\gamma} \to \infty$. The probability distribution of σ at a fixed $\dot{\gamma}$ has a well-defined peak at conditions away from this point but broadens to an essentially flat distribution for $\dot{\gamma} \to \dot{\gamma}_c$ at ϕ_c. The stress fluctuations, determined from force moments on the particles, provide a microscopically based susceptibility, $\hat{\chi}_\sigma \sim \int_{r=2a}^{L/2} \langle \sigma'(\mathbf{x}, t)\sigma'(\mathbf{0}, t)\rangle d^3\mathbf{x}$, with $\mathbf{x}$ being the pair center separation, $r = |\mathbf{x}|$, L the simulation domain size, and σ' the stress fluctuation from $\langle\sigma\rangle$; $\hat{\chi}_\sigma$ displays strong growth on an approach to (ϕ_c, σ_c). An exchange of hydrodynamic for contact stresses is shown to be the basis for the shear thickening, and the relationship of the development of the contact network to the onset of DST is considered. © *2020 The Society of Rheology.* https://doi.org/10.1122/1.5131740

I. INTRODUCTION

In the absence of flow, the microstructural arrangement of particles suspended in viscous liquid is determined by well-established statistical mechanical principles. The influence of temperature, conservative forces, and excluded volume establish an equilibrium state for the particles. By contrast, a nonequilibrium microstructure of sheared suspensions varies depending on the strength of an external driving force. A nonequilibrium suspension microstructure has most commonly been analyzed at the pair distribution level using the Smoluchowksi transport equation, showing pronounced distortion due to the shear flow of the pair-particle distribution function relative to its equilibrium form [1–3]. Such an analysis provides insight into shear thinning and mild shear thickening but has not been extended to the strong shear thickening seen in dense suspensions [4–6], where recent work suggests that a contact between particles is a dominant stress mechanism [7,8] and the network of contacts is microstructurally relevant [9]. These are the conditions of interest in the present study, as we focus on discontinuous shear thickening (DST), in which a large increase in the shear and normal stresses may occur at a fixed shear rate, $\dot{\gamma}$. This implies that the viscosity function $\eta(\dot{\gamma})$ becomes multivalued at some shear rate at a "critical" solid concentration ϕ_c. Most of our attention in this work is devoted to the stress fluctuations in the vicinity of this point. However, we also address briefly the behavior of the contact network near the continuous shear thickening (CST)-DST transition in order to provide some insight into the structural basis for the stress fluctuations.

We consider shear-thickening due to a lubricated-to-frictional (LF) transition in particle interactions [7,10,11], with the transition determined by a characteristic stress defined by a repulsive interparticle force, F_R, and the particle size a as $\sigma_0 = F_R/(6\pi a^2)$. Based on this characteristic stress and the suspending fluid viscosity, η_0, the scale for the shear rate is defined as $\dot{\gamma}_0 = \sigma_0/\eta_0$ and the reported shear rates, denoted by $\dot{\gamma}$, are nondimensionalized by $\dot{\gamma}_0$. Reported viscosities are in the form of a relative viscosity, i.e., the apparent viscosity normalized by η_0. Simulations of the LF transition are well-developed and agree qualitatively with features of experiments [7,10,12]; a brief description appears below.

Our specific purpose is to show that the rapid changes of rheological functions at the onset of DST may be interpreted as a consequence of the presence of a type of critical point. Defining a dimensionless shear stress as $\tilde{\sigma} = \sigma/\sigma_0$, this point is shown as $(\phi_c, \tilde{\sigma}_c)$ on the diagram of flow states in Fig. 1(a). This diagram was proposed by Wyart and Cates (WC) [11] and developed based on simulation data [13]; the diagram shares features with an experimentally determined version based on the behavior of cornstarch dispersions [14]. Flow curves in Fig. 1(b) display $\tilde{\sigma}$ as a function of the dimensionless shear rate, $\dot{\gamma}$, from a fit of these data to the WC mean-field theory [11].

We focus our attention on volume fractions that exhibit strong CST and DST between two flowing states. A key concept is that for particles which interact frictionally, the jamming fraction, ϕ_J^μ, indicated by the vertical line at

Note: This paper is part of the special issue on Physics of Dense Suspensions.
a)Author to whom correspondence should be addressed; electronic mail: morris@ccny.cuny.edu

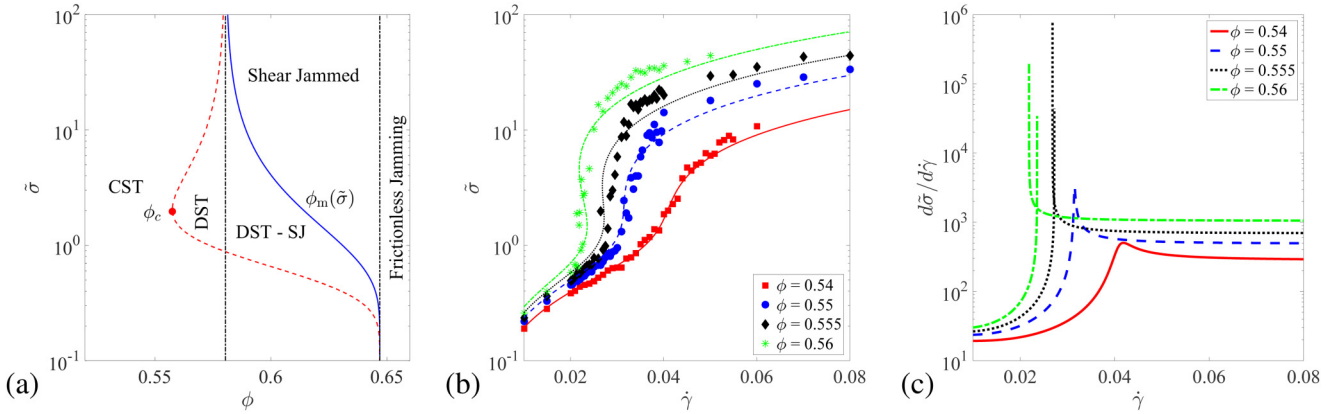

FIG. 1. (a) Flow state diagram, showing the $\phi - \tilde{\sigma}$ values displaying various flow behaviors, with ϕ_c indicated by the (red) dot. The vertical lines at $\phi \approx 0.58$ $\phi \approx 0.65$ indicate the frictional, ϕ_J^μ, and firctionless jamming fraction, ϕ_J^μ, respectively. (b) Stress as a function of shear rate for ϕ near ϕ_c. Points are simulation results, while the lines are the best fit curves for the Wyart–Cates mean field theory [11]. (c) Stress susceptibility, $\partial\tilde{\sigma}/\partial\dot{\gamma}$, from the fits of part (b).

$\phi \approx 0.58$ in Fig. 1(a), lies below its value for frictionless particles, denoted by ϕ_J^0 and indicated by the vertical line to the left of "frictionless jamming" in the same figure. Thus, for ϕ in the range of $\phi_J^0 > \phi > \phi_J^\mu$, discontinuous shear thickening occurs but the thickened state does not have a finite viscosity as it is jammed. We work at conditions below ϕ_J^μ, but the rheology is nonetheless influenced by the different divergences of the viscosity at different stresses, as this provides the mechanism for a stress-driven transition in viscosity, as outlined in the mean-field model fitting of our data in Sec. II and the Appendix.

The curve separating CST and DST is at a solid fraction we label $\phi = \phi_c$, to emphasize that at a particular shear rate the suspension displays a type of critical behavior. This leads to the interpretation that DST is conceptually analogous to a phase transition, albeit far from equilibrium since it arises as a result of varying the external driving. At solid fractions $\phi > \phi_c$, the suspension is able to take on a low- or high-stress state at a given rate of deformation. We describe the behavior in terms of the shear stress σ but could equally use the mean normal stress, or particle pressure [15,16] $\Pi = -(\sigma_{xx} + \sigma_{yy} + \sigma_{zz})/3$ as in the WC formulation [11]. The ratio σ/Π, known as the bulk friction coefficient, undergoes a decrease as the suspension shear thickens [10,17,18], but this decrease is relatively small and thus the strong increase in σ is likewise seen in Π, as shown by Singh *et al.* [13].

Thorough examinations of nonequilibrium phase transitions have been made in various contexts [19], including current-driven steady states of charged particles [20] and ecology models [21]. Here, our goal is more modest, as we cannot assert based on present understanding that the onset of DST has the essential properties of a phase transition. Instead, we are motivated by the fact that, at a critical point, one often observes strong fluctuations to explore the fluctuational characteristics at the onset of DST; our focus in this effort is on the stress fluctuations at fixed shear rate. We begin by considering the mean field description that captures the abrupt rheological transition [11] and then describe the simulation results. The rapid and quite large variations in the stress response at the onset of DST are microscopically associated with the formation and breakage of the flow-driven contact network, and this underlying basis for the rheological response is briefly considered in relation to recent work by a similar approach.

II. MEAN FIELD MODEL

Our work has a twofold motivation, with both arising from a mean-field treatment of the shear-thickening rheology. The first is the success of the WC mean-field theory [11] in capturing the behavior of shear-thickening suspensions [13,22], and the second is the limitation of this approach in capturing statistical physical features associated with fluctuations expected at the apparent critical point.

The WC description reproduces features of CST and DST found in simulations, as shown by Singh *et al.* [13] and illustrated in Fig. 1(b). In WC, the stress is described in terms of the microscopic interactions of close particles, which may be either lubricated or in frictional contact, depending on the imposed stress. The transition away from the low-stress lubricated state occurs when the imposed stress overcomes a repulsive interparticle force, which agrees with the simulation approach [7,10] applied in the current work. The microscopic information that determines the macroscopic flow state in the WC model is the scalar measure f, which gives the fraction of nearest-neighbor interactions that are contacting. This is a mean field model because for fixed global parameters of shear rate (or stress) and solid fraction, f is spatially and temporally uniform. The dependence of the fraction of frictional contacts was described as $f(\Pi)$ in WC, considering Π as the confining normal stress, but we follow Singh *et al.* [13] and write $f(\tilde{\sigma})$ in terms of the shear stress. We use the form found in simulations [10], with $f(\tilde{\sigma})$ being sigmoidal with $f(\tilde{\sigma}) \to 0$ and $f(\tilde{\sigma}) \to 1$ for small and large $\tilde{\sigma}$, respectively. There is a rapid variation near $\tilde{\sigma} \sim 1$.

The suspension rheology is described by considering the two rate-independent limits, lubricated (or frictionless) and frictional, with divergent properties of the form $\eta \sim (\phi - \phi_J)^{-2}$ at their corresponding jamming volume fractions, ϕ_J^0 for $\tilde{\sigma} \ll 1$ and ϕ_J^μ for $\tilde{\sigma} \gg 1$. The jamming fraction varies with imposed stress through a mixing rule using $f(\tilde{\sigma})$ as an interpolant between ϕ_J^0 and ϕ_J^μ, as developed in detail

by Singh *et al.* [13]. The suspension viscosity, η, becomes a function of $\tilde{\sigma}$ only through $f(\tilde{\sigma})$,

$$\eta(\phi, \tilde{\sigma}) = \frac{\alpha^{\mu} f(\tilde{\sigma}) + \alpha^{0}(1 - f(\tilde{\sigma}))}{\left[\phi_{\mathrm{J}}^{\mu} f(\tilde{\sigma}) + \phi_{\mathrm{J}}^{0}(1 - f(\tilde{\sigma})) - \phi\right]^{2}}. \tag{1}$$

This allows us to write the dimensionless shear rate, $\dot{\gamma} = \tilde{\sigma}/\eta(\phi, \tilde{\sigma})$, with $\alpha^{0} \doteq 0.2205$, $\alpha^{\mu} \doteq 0.4850$, $\phi_{\mathrm{J}}^{\mu} \doteq 0.5815$, and $\phi_{\mathrm{J}}^{0} \doteq 0.6470$ for the simulation parameters used in this study. See the Appendix for our fitting to the WC model, with more details of this constitutive model available elsewhere [13].

This rheology exhibits three classes of flow curves, found by seeking fixed points, i.e., $\partial\dot{\gamma}/\partial\tilde{\sigma} = 0$. This reveals a saddle-node bifurcation, with no fixed points for $\phi < \phi_{\mathrm{c}}$, a single fixed point at $(\phi_{\mathrm{c}}, \dot{\gamma}_{\mathrm{c}}, \tilde{\sigma}_{\mathrm{c}})$, and two fixed points for $\phi_{\mathrm{c}} < \phi < \phi_{\mathrm{J}}^{\mu}$. This can be stated in terms of the material response. For $\phi < \phi_{c}$, the stress is a single-valued function of the shear rate for all shear rates, corresponding to CST. For $\phi_{\mathrm{c}} < \phi < \phi_{\mathrm{J}}^{\mu}$, the model predicts S-shaped flow curves so that $\tilde{\sigma}$ can have three possible values for a fixed shear-rate: this is the DST region. For $\phi > \phi_{\mathrm{J}}^{\mu}$, there is only one flowing state fixed point, as thickening here gives rise to shear jamming [DST-SJ, as shown in Fig. 1(a)].

The saddle node bifurcation thus has a clear analogy to the behavior predicted by a cubic, e.g., van der Waals, equation of state. As the volume fraction increases in Fig. 1(b), the first point at which $\partial\tilde{\sigma}/\partial\dot{\gamma} \to \infty$ is then analogous to a critical point. Such a state is expected to be associated with strong fluctuations in certain properties. With this in mind, rather than analyzing $\partial\dot{\gamma}/\partial\tilde{\sigma}$ to find fixed points of a dynamical system, $\partial\tilde{\sigma}/\partial\dot{\gamma}$ is interpreted as the stress susceptibility. Such an interpretation identifies $\tilde{\sigma}$ as an order parameter, and the WC model predicts a susceptibility divergence $\chi_{\sigma} = \partial\tilde{\sigma}/\partial\dot{\gamma} \to \infty$ at a point $(\phi_{\mathrm{c}}, \dot{\gamma}_{\mathrm{c}}, \tilde{\sigma}_{\mathrm{c}})$, as suggested by Fig. 1(c). These data tend toward the low- and high-shear rate viscosity in the appropriate limits but exhibit growth to a maximum at an intermediate value of $\dot{\gamma}$. A divergence in the susceptibility, $\chi_{\sigma} \to \infty$, is found for $\phi_{\mathrm{c}}^{\mathrm{MF}} \doteq 0.552$ and $\dot{\gamma}_{\mathrm{c}}^{\mathrm{MF}} \doteq 0.0296$ from our fitting of simulation data of this study to the WC theory; the superscript MF is used to emphasize that these are the values extracted from our application of the mean-field theory. Based on these values, $\chi_{\sigma} \sim (\dot{\gamma} - \dot{\gamma}_{\mathrm{c}})^{-b}$ near $\dot{\gamma}_{\mathrm{c}}$ with $b \doteq 0.680$ for $\dot{\gamma} > \dot{\gamma}_{\mathrm{c}}$ and $b \doteq 0.653$ for $\dot{\gamma} < \dot{\gamma}_{\mathrm{c}}$; these exponents are notably close to $2/3$ but are determined numerically as described in the Appendix.

The relationship of the apparent critical point to the suspension properties accords with certain expectations for an equilibrium thermodynamic critical point. As ϕ increases, the curves go from CST to DST at ϕ_{c}. Similar behavior is seen experimentally [4–6,23] for either viscosity or stress as a function of $\dot{\gamma}$. In addition to this average behavior, strong fluctuations are seen experimentally [24–26] in the time series of σ. In Boersma *et al.* [24], very concentrated ($\phi \doteq 0.585$) monodisperse polystyrene spheres in water-glycerine mixtures underwent viscosity fluctuations of over an order of magnitude, with long periods in either the high- or low-stress state as $\dot{\gamma}$ approached the transition from below, although it is unclear whether this condition is near the onset of DST or fully in that regime. Addressing fluctuations requires a microscopic view of the material, which we obtain from simulation, where we can access the temporal and spatial stress fluctuations at the particle level directly.

III. SIMULATIONS

For this study, we report on discrete-particle simulations near the critical point as identified by the fitting of the WC theory, in the range of $0.54 \leq \phi \leq 0.56$. The simulation method is the lubricated flow-discrete element model (LF-DEM) [7,10]. This method considers spherical particles immersed in a Newtonian liquid that lubricates the particle surfaces at low stress but neglects long-range hydrodynamic interactions. Motivated by the concept of "lubrication breakdown," the failure of hydrodynamic lubrication to maintain finite surface separation in sheared dense suspensions as shown by Ball and Melrose [27], a key feature is that the method allows for frictional contact interactions between particles when the imposed shearing force overwhelms a repulsive interparticle force.

The particles are bidisperse, with radii $a_1 = a$ and $a_2 = 1.4a$, to avoid ordering observed in dense monodisperse suspensions [28]. Half of the total solid volume is contributed by particles of each radius. The $N = 500$ particles are confined to a cubic unit cell of volume V fixed by the desired value of ϕ. The unit cell is periodically replicated in all three directions and sheared according to Lees-Edwards boundary conditions. The simulations reported were performed at an imposed shear rate, with the shear stress fluctuating.

We consider conditions of zero inertia so that each particle satisfies a balance between finite-range hydrodynamic ($\mathbf{F}_{\mathrm{H}}$) and conservative forces ($\mathbf{F}_{\mathrm{R}}$), as well as contact forces ($\mathbf{F}_{\mathrm{C}}$). Here, we use what is termed the critical load model [7] to capture the influence of the repulsive forces: in this case, we do not have finite-range repulsion, but instead impose a threshold contact normal force denoted by F_R to indicate its role in replacing the repulsion; above this normal force, friction is activated in the contact force. The particles thus obey the force balance

$$0 = \mathbf{F}_{\mathrm{H}} + \mathbf{F}_{\mathrm{C}}, \tag{2}$$

along with a similar torque balance involving hydrodynamic and frictional torques. The hydrodynamic force $\mathbf{F}_{\mathrm{H}}$ accounts for lubrication, which is associated with the fluid in the zone of closest approach of neighboring particle surfaces and is the dominant pair hydrodynamic interaction for the volume fractions of interest, as well as single-particle Stokes drag [7]. We write the lubrication for a generic pair of particles labeled i and j as $\mathbf{F}_{\mathrm{H}} = -\mathbf{R}_2(h) \cdot (\mathbf{U}_j - \mathbf{U}_i)$, with the pair resistance tensor $\mathbf{R}_2 \sim (h + \delta)^{-1}$, where $h = r - (a_i + a_j)$; δ restricts the lubrication resistance to be finite at contact ($h = 0$) and can be considered as representative of a roughness scale, but without any further physical modeling of roughness. When contact occurs, the contact force, $\mathbf{F}_{\mathrm{C}}$, comes into play. When the interparticle normal force exceeds the value F_R, friction is activated, and satisfies the Coulomb criterion, $F_{\mathrm{C,t}} \leq \mu F_{\mathrm{C,n}}$, relating tangential ($F_{\mathrm{C,t}}$) and normal

($F_{C,n}$) components. We study only $\mu = 1$ here. Prior work has shown that varying μ alters the frictional jamming fraction and the volume fraction for DST [7,13], leaving the overall physical scenario intact.

The relative viscosity η_r and the normal stress differences fluctuate rather strongly in the region of strong shear thickening, as described in an initial work with LF-DEM [7]. For viscosity, this is qualitatively in accordance with experimental observations [24,25]. A caveat regarding comparison of simulation and experimental data is that our simulations are performed in periodic domains without walls, while the experiments have solid boundaries in the gradient direction.

The appearance of fluctuations in the viscosity indicates a growing susceptibility to shear stress. We formalize the concept by defining this susceptibility as $\chi_\sigma = \partial\langle\tilde{\sigma}\rangle/\partial\dot{\gamma}$, with the angle bracket defining an ensemble average over the nonequilibrium steady state. Strong fluctuations are typically observed at a thermodynamic critical point, and the susceptibility can be related to the correlation of fluctuations in the relevant order parameter. This microscopic basis for the behavior is not accessible to the mean-field model, which may nonetheless exhibit a divergent χ_σ as shown by Fig. 1(c) (i.e., the divergence may be predicted in mean field but is typically associated with and altered by the "critical state fluctuations"). We show that the susceptibility χ_σ defined in terms of stress fluctuations exhibits strong growth as $\dot{\gamma} \to \dot{\gamma}_c$ for $\phi = \phi_c$.

The fluctuations of the shear stress are shown in a time series or more precisely as a function of strain $\gamma = \dot{\gamma}t$, in Fig. 2(a) for $\phi = 0.55$ and in Fig. 2(b) for $\phi = 0.56$. Among the conditions plotted, that closest to the apparent critical point, i.e., the point at which DST is first observed, is $\phi = 0.55$ and $\dot{\gamma} = 0.0355$. At this condition, σ varies frequently between the high- and low- stress states, spending little time in a given state. For the suspension studied here, we identify the approximate values, based on the stress statistics, of $\phi_c \doteq 0.55$ and $\dot{\gamma}_c \doteq 0.0315$. Recall that the values obtained from a mean field fitting are $\phi_c^{MF} \doteq 0.552$ and $\dot{\gamma}_c^{MF} \doteq 0.0296$. For $\phi = 0.56$ in Fig. 3(b), for $\dot{\gamma} = 0.025$, the system spends significant time in both high- and low-stress states, indicating that this condition is in the two-state portion of the material response, i.e., it is fully within the DST regime.

A. Stress distributions

We determine the probability distribution for the time series of the total shear stress (as shown in Fig. 2) and denote this $P(\tilde{\sigma})$. This is found by sampling $\tilde{\sigma} = V^{-1}\sum_i^N \tilde{\sigma}_i$ at intervals of 0.01 strain for 20 strain units after reaching a steady state; $\tilde{\sigma}_i$ is the shear stress contribution by particle i, determined as the appropriate component of the force moment $\tilde{\sigma}_i = -\sum_j \mathbf{x}_{ij}\mathbf{F}_{ij}$ with j denoting the close neighbors, $\mathbf{x}_{ij}$ the center separation vector of i and j, and $\mathbf{F}_{ij}$ all of the lubrication and contact forces for this pair.

We focus on $\phi = 0.55$ and $\phi = 0.56$ to illustrate the primary features of the probability distributions of the bulk shear stress, $P(\tilde{\sigma})$. Figure 3(a) shows $P(\tilde{\sigma})$ for $\phi = 0.55$ ($\approx \phi_c$). For the lowest $\dot{\gamma}$, for which the suspension is in the low-stress state with lubricated interactions, $P(\tilde{\sigma})$ is relatively narrow with an average value near a well-defined peak. As $\dot{\gamma}$ increases toward the transition, the peak of the distribution shifts to larger values of $\tilde{\sigma}$ and the symmetry of the distribution is broken with the emergence of a larger tail for $\tilde{\sigma} > \langle\tilde{\sigma}\rangle$, indicating that the stress has a baseline value but makes occasional excursions to much larger stress; certain features of the stress probability distribution agree with the experimental findings presented in Lootens *et al.* [25]. When the shear rate approaches the critical point, this tail becomes more pronounced. The distribution closest to $\dot{\gamma} = \dot{\gamma}_c$ is nearly flat, i.e., the system does not remain in states near the mean stress, but samples from a wide range almost uniformly, as expected at a critical point. Results of Lootens *et al.* do not show a flat probability distribution, possibly indicating that they sampled at ϕ away from ϕ_c, and boundary effects in the experiments cannot be discounted.

As the value of $\dot{\gamma}$ passes $\dot{\gamma}_c$, the reverse trend is observed. The low stress values in the distribution become less frequent, and the large-$\tilde{\sigma}$ peak becomes dominant. The distribution is wider for the high stress state.

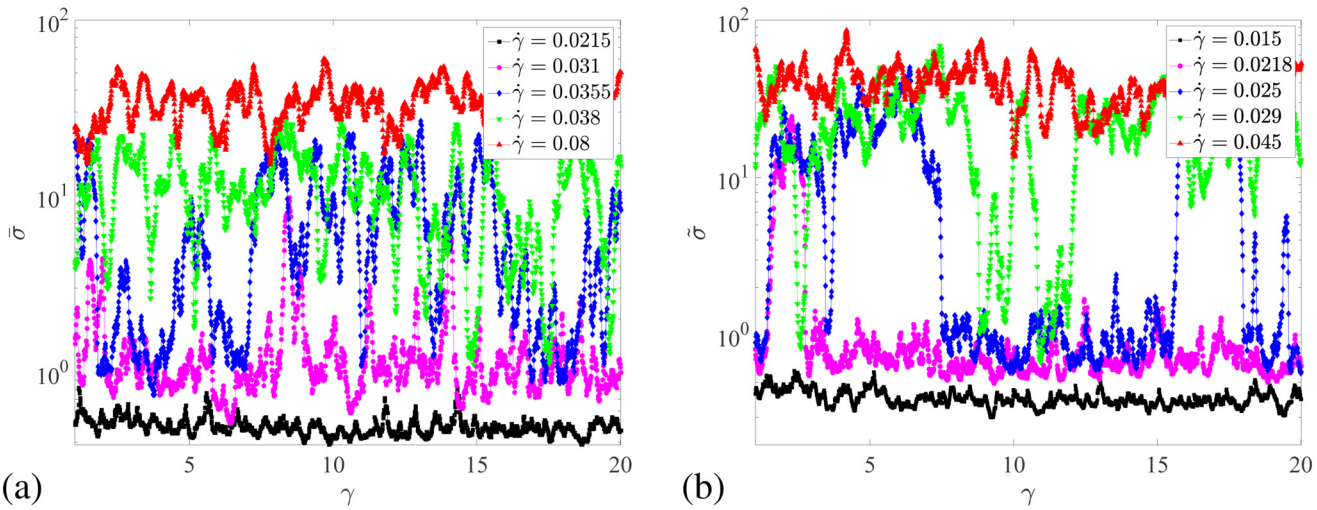

FIG. 2. Shear stress, $\tilde{\sigma}$, as a function of strain, $\gamma = \dot{\gamma}t$, for several imposed shear rates $\dot{\gamma}$ at (a) $\phi = 0.55$ and (b) $\phi = 0.56$.

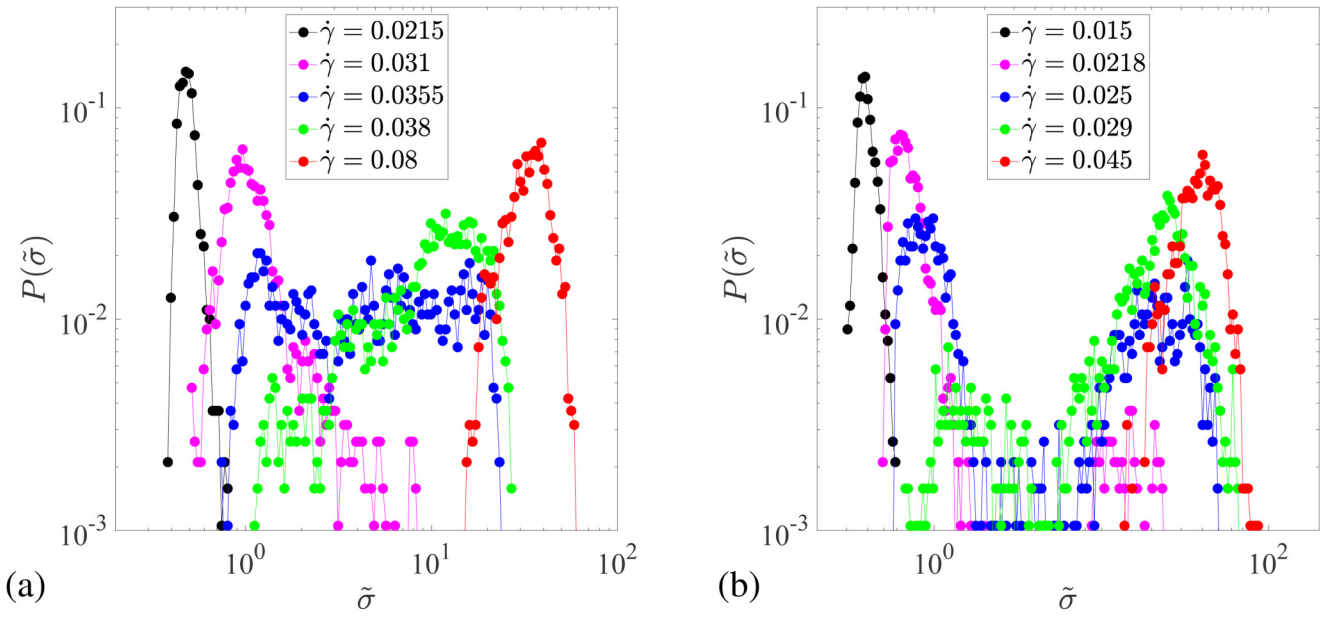

FIG. 3. Shear stress distribution for several imposed shear rates $\dot{\gamma}$ at (a) $\phi = 0.55$ and (b) $\phi = 0.56$.

Now we consider $\phi = 0.56$, which is greater than ϕ_c and well into the DST zone. The distributions shown in Fig. 3(b) for low and high stress are similar to the forms at $\phi = 0.55$. However, we observe a new feature, as the distribution does not become flat, but instead the large-$\tilde{\sigma}$ tail seen on approach to the transition splits off: the distribution exhibits two separate peaks with a region of vanishing probability between. This peak at larger stress grows with increasing $\dot{\gamma}$ at the expense of the small-stress portion of the distribution. Ultimately, the portion of the distribution at low stress disappears, and we end up with a single distribution for the high-stress state. The splitting of the distribution indicates temporal exchange of low- and high-stress states (or "phases") during the transition. This is again reminiscent of the experimental data of Boersma *et al.* [24], although we once more point out that the boundaries may play a role in the experimental behavior.

We return now to the time series of the stress associated with the $P(\tilde{\sigma})$ plots in Fig. 3 shown for $\phi = 0.55$ in Fig. 2(a) and $\phi = 0.56$ in Fig. 2(b). At the higher volume fraction, the stress is seen to occupy a distinct high or low value, with sharp jumps between the two, with long periods at either level for the intermediate shear rates. In contrast to this, for $\phi = 0.55$ at the transition from low to high stress, which occurs for values of the dimensionless shear rate near $\dot{\gamma} = 0.0355$, $\tilde{\sigma}$ is seen to spend time at all values in its range, and $P(\tilde{\sigma})$ confirms that at this shear rate, there is no preferred value of the stress.

The particle pressure is the mean particle-phase normal stress, $\Pi = -(\sigma_{xx} + \sigma_{yy} + \sigma_{zz})/3$, a quantity which has been termed the nonequilibrium osmotic pressure [15]. The interparticle forces which are the mechanical basis for this pressure are driven by the shearing motion, and thus Π varies with $\dot{\gamma}$. Probability distributions of $\tilde{\Pi} = \Pi/\sigma_0$ are shown in Fig. 4(a) for $\phi = 0.55$ and for $\phi = 0.56$ in Fig. 4(b). These demonstrate the same hallmarks of the critical region as does the shear stress distribution: near the critical point, $P(\tilde{\Pi})$ is nearly flat, and for $\phi > \phi_c$, we observe a bimodal distribution of $\tilde{\Pi}$ as the result of occupying two distinct states at a fixed $\dot{\gamma}$. The probability distribution of Π is quite similar to that of the shear stress, displayed in Fig. 3, and the time series is also similar and is not displayed.

B. Exchange of dominant stress mechanism

For the suspension simulated, the stress arises from two mechanisms, contact ($\tilde{\sigma}_c$) and hydrodynamic ($\tilde{\sigma}_H$). Rather than implementing a finite-range repulsive force, the influence of F_R is captured through the critical load model, in which frictional forces arise only when the contact normal force exceeds a threshold; thus the stress due to repulsive force is captured by the contact stress. The stress is computed as the moment of the lubrication or contact forces between neighboring particle surfaces, i.e., for the contact stress this is given by $\sigma_c^i = -\sum_j \mathbf{x}_{ij}\mathbf{F}_c^{ij}$, with j labeling the close near neighbors of particle i.

The two stress contributions are shown as a fraction of the total stress ($\tilde{\sigma}$) for three different volume fractions in Fig. 5. An exchange between these two mechanisms is observed during the shear thickening transition. As $\dot{\gamma} \to 0$, hydrodynamic stress is the only mechanism: $\tilde{\sigma}_H/\tilde{\sigma} \to 1$ and $\tilde{\sigma}_c/\tilde{\sigma} \to 0$. The increase in suspension viscosity at the onset of shear-thickening is associated with development of the contact stress, and the abrupt upturn at DST is found to occur, for $\phi = 0.55$, when $\tilde{\sigma}_c/\tilde{\sigma} \approx 0.42$, with a similar value associated with the abrupt jump at $\phi = 0.555$. As $\dot{\gamma} \to \infty$, the hydrodynamic fraction of the total stress becomes very small but remains finite for the volume fractions considered since the suspension is able to flow. A vanishing hydrodynamic stress implies shear jamming as developed by Seto *et al.* [29].

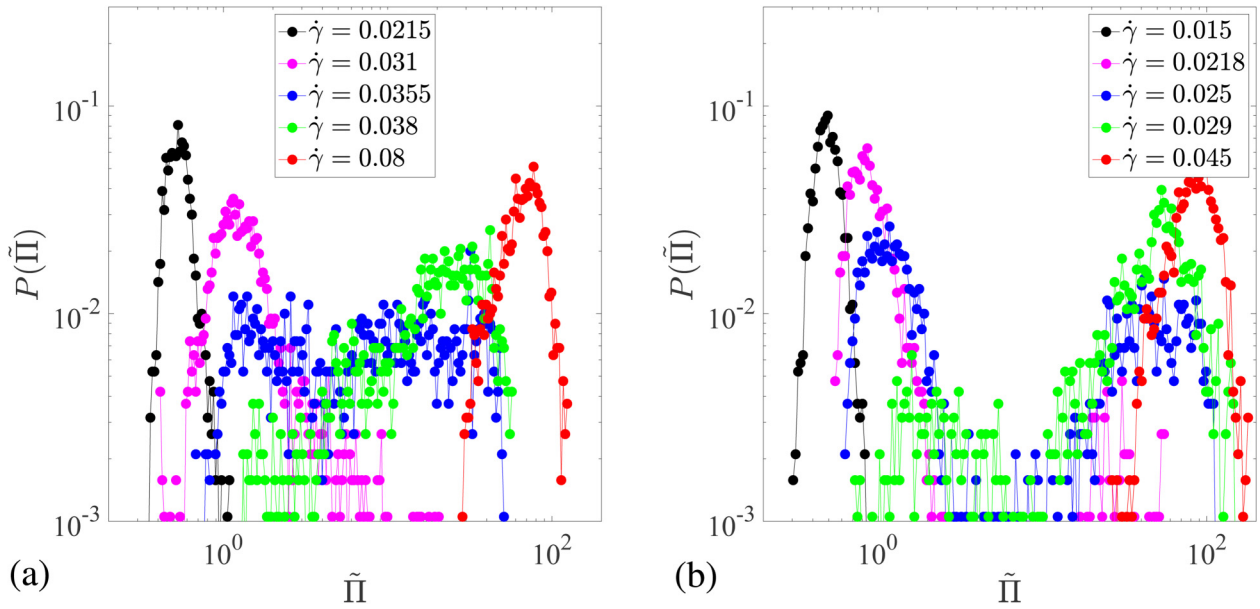

FIG. 4. Particle pressure distributions for varying shear rate $\dot{\gamma}$ at (a) $\phi = 0.55$ and (b) $\phi = 0.56$.

C. Stress correlations

We calculate the spatial correlations of the shear stress fluctuations, $\tilde{\sigma}$, as

$$S(\mathbf{r}) = \sum_{i}^{N} \sum_{j \neq i}^{N} \frac{\sigma_i'(\mathbf{r}_i, t)\sigma_j'(\mathbf{r}_j, t)\delta(\mathbf{r} + \mathbf{r}_j(t) - \mathbf{r}_i(t))}{\langle \sigma_i \rangle \langle \sigma_j \rangle}, \qquad (3)$$

where σ_i' denotes a fluctuation of the stress contribution from its ensemble average $\langle \sigma_i' \rangle$. Note that the subscript on, for example, σ_i indicates a particle stress (force moment); this is not the bulk stress, which arises from the sum of these moments. Since the system studied is translationally invariant, the correlations are a function of center separation. Thus, we write $\mathbf{x} = \mathbf{r}_i - \mathbf{r}_j$ and the fluctuations as $\sigma_i'(\mathbf{x}, t) = \tilde{\sigma}_i(\mathbf{x}, t) - \langle \tilde{\sigma}_i \rangle$. Angularly averaged correlations, $\langle S(r) \rangle$ with $r = |\mathbf{x}|$, are presented in Fig. 6. While the correlations have angular variations, we here present only the angularly averaged form. Over the entire domain, the correlations grow to their largest value in the shear rate range from $\dot{\gamma} \approx 0.031$ to 0.0355 and then decay for larger $\dot{\gamma}$. The radial variation of these correlations is similar and long-ranged for all conditions, with temporal fluctuations pronounced near $\dot{\gamma}_c$; the small size of our simulations, with $N = 500$ in the replicated unit cell, may lead to coherent fluctuations over the entire domain such that only temporal fluctuations are observed.

Recall that thermodynamic susceptibilities can be related to fluctuations [30]. We use this as the motivation for considering the fluctuations in the individual particle stress contributions as the microscopic basis of the stress susceptibility. We define a fluctuation-based susceptibility as the volume integral of the appropriate stress fluctuation correlations normalized by the system volume, $\hat{\chi}_\sigma = \hat{V}^{-1} \int_{r=2a}^{L/2} \langle \sigma'(\mathbf{x}, t)\sigma'(\mathbf{0}, t) \rangle d^3\mathbf{x}$, where $\hat{V} = \int_{r=2a}^{L/2} d^3\mathbf{x}$; we distinguish this microscopically defined susceptibility with the hat notation.

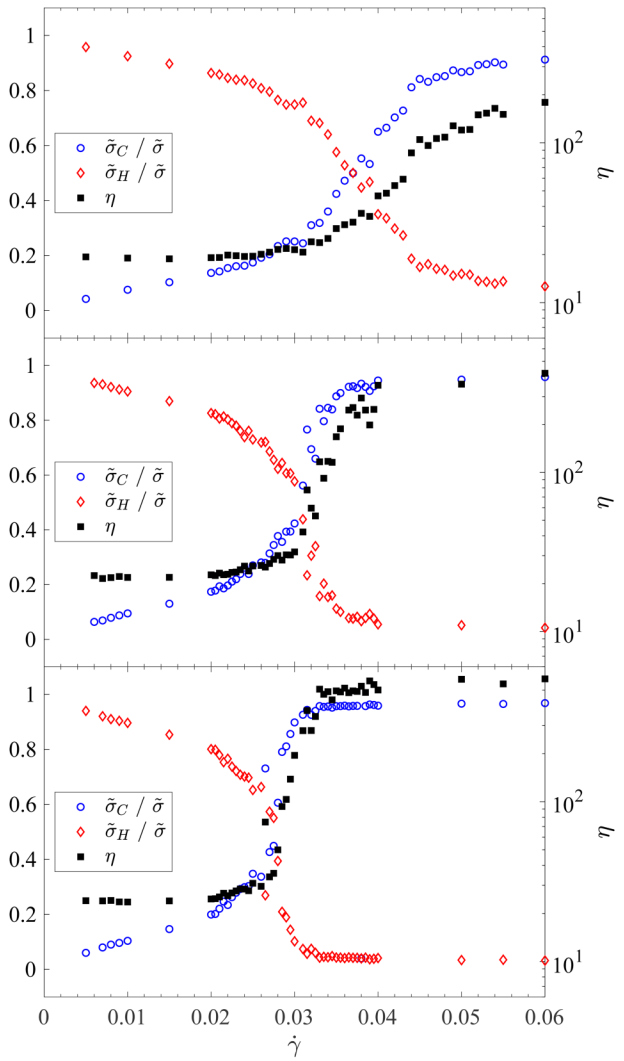

FIG. 5. The fraction of stress from hydrodynamic, $\tilde{\sigma}_H/\tilde{\sigma}$, or from contact, $\tilde{\sigma}_C/\tilde{\sigma}$, contributions plotted on the left axis, along with η plotted on the right axis, for (top) $\phi = 0.54$, (middle) $\phi = 0.55$, and (bottom) $\phi = 0.555$.

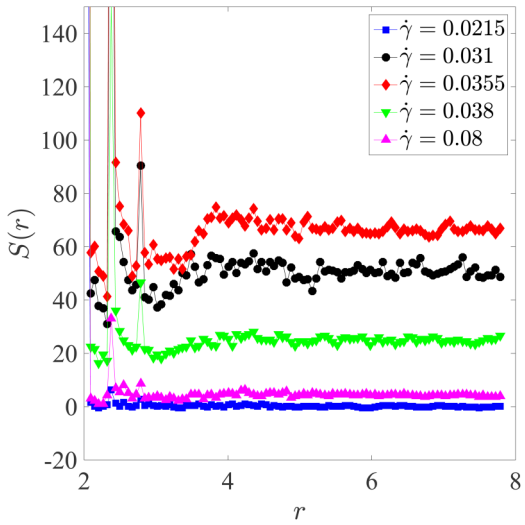

FIG. 6. Angular average of the shear stress correlation, $\langle S(\mathbf{r})\rangle$ as a function of $\mathbf{r}$ for $\phi = 0.55$.

The results of the integrations are presented in the middle plot of Fig. 7 and show that $\hat\chi_\sigma$ grows strongly at shear rates where $\partial\tilde\sigma/\partial\dot\gamma \to \infty$. The microscopic susceptibility becomes sharply peaked at its highest value for $\phi = 0.55$ and $\dot\gamma = 0.0315$. As noted above, we identify this pair of values as $(\phi_c, \tilde\sigma_c)$. This point also corresponds to the inflection of

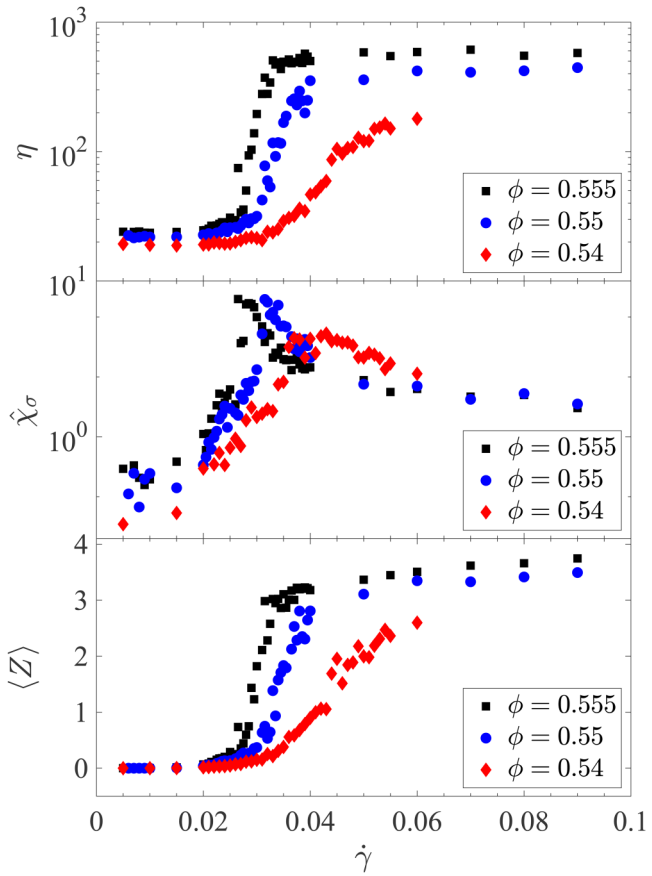

FIG. 7. Top: suspension viscosity, η; middle: the microscopic (fluctuationally defined) stress susceptibility, $\hat\chi_\sigma$; bottom: the average frictional coordination number, $\langle Z\rangle$, in the same range of $\dot\gamma$, near the apparent critical point.

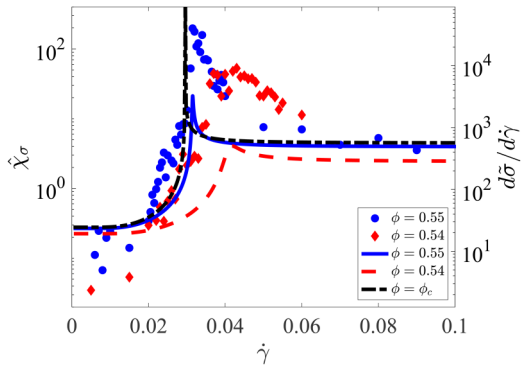

FIG. 8. Comparison of $\hat\chi_\sigma$ (represented by dots) with the mean field $\partial\langle\tilde\sigma\rangle/\partial\dot\gamma$ (represented by lines) for $\phi = 0.54$ and $\phi = 0.55$. Note that from the mean field analysis, $\partial\langle\tilde\sigma\rangle/\partial\dot\gamma$ diverges at $\phi = \phi_c^{\mathrm{MF}} \doteq 0.552$ and $\dot\gamma_c^{\mathrm{MF}} \doteq 0.0296$.

the viscosity η as a function of $\dot\gamma$, as can be seen in the top of Fig. 7, and is close to the shear rate for which a flat $P(\tilde\sigma)$ is observed in Fig. 3. The microscopic $\hat\chi$ is compared with the mean field susceptibility $\partial\langle\tilde\sigma\rangle/\partial\dot\gamma$ in Fig. 8. This figure, which also includes the divergent ϕ_c mean field susceptibility, illustrates that the microscopic (fluctuational) susceptibility grows strongly in the same shear rate range as the mean field version but with a broader peak. The peak broadening may be influenced by the small size of the simulated system.

It is important to note that in our definition of the stress fluctuations, taken relative to the ensemble average within the steady state, the fluctuations are primarily temporal as the entire system changes the stress level, although there remains a dispersion around that level. We do not identify a growing length scale at the transition, but instead there is a system-spanning correlation at all conditions. The precise basis for this behavior is not clear but, as noted above, it seems likely to be due to the smallness of the system size ($N = 500$, and thus about eight particle diameters in the linear dimension of the unit cell) leading to coherent stress fluctuations across the entire volume simulated.

D. Frictional contact network

The sudden and rather extreme changes in the rheology seen in the temporal fluctuations near DST can be associated with changes in the interparticle contact state, which is captured in a mean-field sense by the fraction of frictional contacts f in the WC theory. A more detailed description is provided by considering the frictional contact network, where the particle centers are the vertices and the frictional contacts form the edges of the network. Such methods have been considered previously for dense suspensions [9,31]. The adjacency matrix corresponding to this undirected network is the $N \times N$ symmetric A_{ij}, where N is the number of particles: there is a frictional contact between particles i and j, then $A_{ij} = 1$, otherwise $A_{ij} = 0$. At a given instant, the contact number of a particle is $Z_i = \sum_j^N A_{ij}$, and the mean degree of the frictional contact network is $Z = \sum_i Z_i/N$; the squared contact number is $\sum_i Z_i^2/N$. We determine $\langle Z\rangle = \langle\sum_i Z_i/N\rangle$ and $\langle Z^2\rangle = \langle\sum_i Z_i^2/N\rangle$ as their sampled averages over many configurations. The variation of $\langle Z\rangle$ with shear

rate for three volume fractions ϕ near the critical value is shown in Fig. 7, with the viscosity and the microscopic stress susceptibility curves plotted directly above. $\langle Z \rangle$ is closely linked with the stress state of the suspension, showing a parallel trend to the low- to high-viscosity transition. The low-viscosity (small $\dot{\gamma}$) state is associated with $\langle Z \rangle = 0$, and $\langle Z \rangle$ reaches its highest value (depending on ϕ) as $\dot{\gamma} \to \infty$, when the suspension reaches the high-viscosity state. It is thus clear that, in the LF scenario, the formation of frictional contacts is essential for development of the high-stress state of the system. This agrees with Fig. 5, which showed that DST is associated with a rapid exchange of stress mechanism, with the important feature that there is a discontinuous rise in the fraction of the stress contributed by the contact forces.

However, the relationship of the contact network to DST is somewhat subtle. In recent network theoretical analysis of shear thickening in suspensions [9], it was suggested that the formation of a percolating frictional network, or a "giant connected component" in the graph theory terminology, was responsible for the transition from CST to DST. We show that this is not accurate for the present simulations. To do so, we first determine the fraction of the total particles in the largest frictionally contacting cluster, whose average $\langle p \rangle$ is displayed as a function of $\dot{\gamma}$ for $\phi = 0.55$ in Fig. 9 at top. Here, a clear correlation of the growth of the largest contacting cluster with the increase in viscosity is seen. However, the Molloy–Reed (MR) criterion for the development of a giant component in a random network, namely, that the second-nearest neighbors outnumber the near neighbors, implies that $\langle Z^2 \rangle - 2\langle Z \rangle$ vanishes at the contact percolation [32,33]. Dorogovtsev *et al.* [32] show that the size of a connected cluster as $\langle Z \rangle$ increases is given by $s \equiv 1 + \langle Z \rangle^2 / (2\langle Z \rangle - \langle Z^2 \rangle)$ and based on the Molloy–Reed criterion should diverge at the value of the shear rate corresponding to

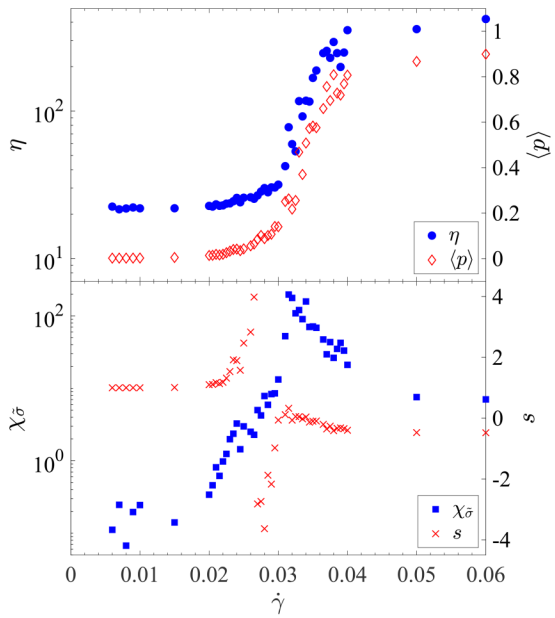

FIG. 9. Top: viscosity, η, and the average fraction of particles in the largest frictional cluster, $\langle p \rangle$; bottom: microscopic (fluctuationally defined) stress susceptibility, $\hat{\chi}_\sigma$, and the quantity s (defined and described in the text) which diverges at contact percolation, for $\phi = 0.55$.

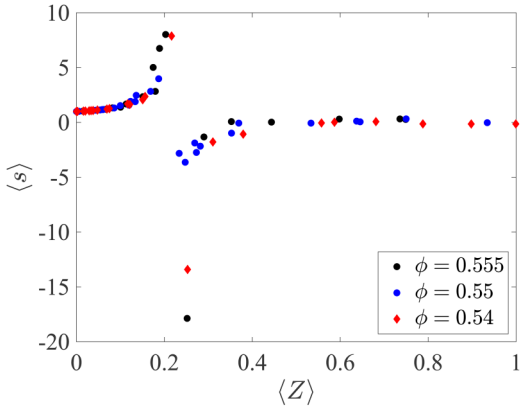

FIG. 10. The quantity s (see text) which indicates the mean size of a frictional cluster below its divergence, as a function of the mean frictional coordination number, $\langle Z \rangle$. Note that values for only small values of the coordination number, $\langle Z \rangle < 1$, are plotted.

the emergence of this system-spanning cluster, known as a giant component in network theory [32,34]. While it is unclear whether the MR criterion developed for uncorrelated networks with arbitrary degree distributions can be directly used for the network of contacts in the sheared suspension, we plot the quantity s in Fig. 9 (at bottom) along with the fluctuationally defined $\hat{\chi}_\sigma$ previously shown to be maximized where the viscosity undergoes its steepest increase in Fig. 7. It is seen that s diverges, or contact percolation may be assumed to occur in some direction if this network follows the results developed for uncorrelated networks (by no means certain, as noted), at a shear rate lower than $\dot{\gamma}_c$, at which $\hat{\chi}_\sigma$ is maximized, indicating that the MR criterion does not strictly determine the onset of DST. We can safely say that network criticality associated with percolation of contacts (the formation of a giant component) does not correspond to the "rheological critical point" associated with the onset of DST, a correspondence that was previously suggested [9]. To make this point more firmly and simply, note that frictional contact percolation and the giant connected component can be found even under CST conditions, as shown for $\phi = 0.54$ in Fig. 10; direct analysis of the percolation threshold confirms that percolation occurs in all directions at $\phi = 0.54$, but at a shear rate higher than the divergence of s, independent of the applicability of network theory results to this system. Note that in this figure, only small values of the coordination number, $\langle Z \rangle \leq 1$, are considered, although the value goes up to $\langle Z \rangle > 3$ at high stress.

IV. DISCUSSION AND CONCLUDING REMARKS

We have explored the fluctuations in stress at the onset of DST in dense suspensions. This is motivated by the divergence in the rate of increase of stress with shear rate, $\partial\sigma/\partial\dot{\gamma}$, which in the mean field description is a saddle-node bifurcation but may be considered as analogous to a second-order phase transition at which critical fluctuations may be expected. In fact, strong fluctuations in the shear and normal stress are seen when the suspension is driven at a fixed shear rate near the onset of DST. We have focused here on the apparent critical point for the transition from low- to

high-viscosity states on the volume fraction-shear stress (ϕ-$\tilde{\sigma}$) plane and have shown that the region around this point (ϕ_c, $\dot{\gamma}_c$) has large susceptibility to temporal stress fluctuations. The stress fluctuations from simulation have qualitative similarity with experimental results for spherical particles [24,25] and recent work by Hermes *et al.* [26] with corn starch dispersions, which specifically targeted the DST regime. We caution that numerous aspects in the experiments may be absent or differ in the simulations, making a direct comparison difficult.

From our work, the clear role of a rapid exchange of the dominant stress mechanism from hydrodynamic to frictional has been elucidated, and the probability distributions of the stress response of the suspension have been probed. The stress is found to be distributed around well-defined peaks away from the DST transition, but it exhibits a shoulder indicative of excursions to large stress upon an approach to transition, and a broad flat distribution near (ϕ_c, $\dot{\gamma}_c$).

As our system size is quite small, with $N = 500$ particles in the periodically replicated simulational unit cell, our ability to explore spatial correlations of the fluctuations of stress is limited. It appears that, for this small value of N, stress fluctuations are correlated across the flow domain, leading to the dominant fluctuations being temporal. Larger systems can be studied without extreme computational expense if systematic analysis of the size dependence is applied only at conditions very near the apparent critical point for onset of DST, and this could provide valuable insight into the form of the growth and potential divergence of the simulationally determined stress susceptibility. The strong stress fluctuations are conjectured to be due to an extreme sensitivity to the addition or removal of individual frictional contacts as the suspension flows, as this can cause major changes in the size of a connected component in the force network and thus strongly alter the total stress the suspension is able to exert at a fixed shear rate. Our own examinations of the network properties of the shear-thickening suspension are motivated by the insights gained from this approach by Boromand *et al.* [9]. We find similar behaviors to that study, but some differences have been noted; in particular, we find that percolation of frictional contacts can occur for both strong CST and DST, and thus the onset of contact percolation does not imply the onset of DST. Further work examining the detailed relationship of the force network to the stress response in suspensions is warranted.

ACKNOWLEDGMENT

This work was supported by the National Science Foundation (NSF) (Nos. 1605283 and 1916879).

APPENDIX: WC MODEL—RHEOLOGICAL FITTING AND BIFURCATION ANALYSIS

First, we describe the fitting of the simulation data to the WC model [11] using the procedure of Singh *et al.* [13]. The rate-independent relative viscosities (normalized by the pure fluid viscosity) at low- and high-stress conditions are expressed as $\eta^L(\phi) = \alpha^0(\phi_J^0 - \phi)^{-2}$ and $\eta^H(\phi, \mu) = \alpha^\mu(\phi_J^\mu - \phi)^{-2}$, where α^0 and α^μ are constant coefficients, while ϕ_J^0 and ϕ_J^μ denote the frictionless and frictional jamming volume fractions, respectively. Figure 11(a) shows the fit of the simulation data at low- and high-stress conditions with $\alpha^0 = 0.2205$, $\alpha^\mu = 0.4850$, and $\phi_J^0 = 0.647$, $\phi_J^\mu = 0.5815$. The interparticle friction coefficient is $\mu = 1$, and simulation is by the "critical load model" [7].

Next, the stress dependent jamming packing fraction and the coefficients are expressed as $\phi_m(\tilde{\sigma}) = \phi_J^\mu f(\tilde{\sigma}) + \phi_J^0[1 - f(\tilde{\sigma})]$ and $\alpha_m(\tilde{\sigma}) = \alpha^\mu f(\tilde{\sigma}) + \alpha^0(1 - f(\tilde{\sigma}))$, where $f(\tilde{\sigma})$ denotes the fraction of frictional contacts. Figure 11(b) shows $f(\tilde{\sigma})$ to be largely independent of volume fraction, and the simulation data are fitted to the sigmoidal function, $f(\tilde{\sigma}) = \exp\left[-\tilde{\sigma}^*/\tilde{\sigma}\right]$, with $\tilde{\sigma}^* = 1.87$.

Finally, the dependence of η on $\tilde{\sigma}$ and ϕ is expressed as $\eta(\phi, \tilde{\sigma}) = \alpha_m(\tilde{\sigma})[\phi_m(\tilde{\sigma}) - \phi]^{-2}$, which is shown in an expanded form as Eq. (1) in the main text, combining the expressions for ϕ_m, α_m, and $f(\tilde{\sigma})$. Figure 11(c) shows η as a function of shear stress $\tilde{\sigma}$ for different ϕ.

Next, we briefly describe the analysis for determining the fixed points $\partial\dot{\gamma}/\partial\sigma = 0$. The expression for $\dot{\gamma} = \sigma/\eta(\sigma, \phi)$ using (1) may be written as

$$\dot{\gamma} = \frac{\sigma[f(\sigma)(\phi_J^\mu - \phi_J^0) + (\phi_J^0 - \phi)]^2}{f(\sigma)(\alpha^\mu - \alpha^0) + \alpha^0}. \tag{A1}$$

Defining

$$h(\sigma) = [f(\sigma)(\phi_J^\mu - \phi_J^0) + (\phi_J^0 - \phi)]^2, \tag{A2}$$

$$g(\sigma) = f(\sigma)(\alpha^\mu - \alpha^0) + \alpha^0, \tag{A3}$$

we can write

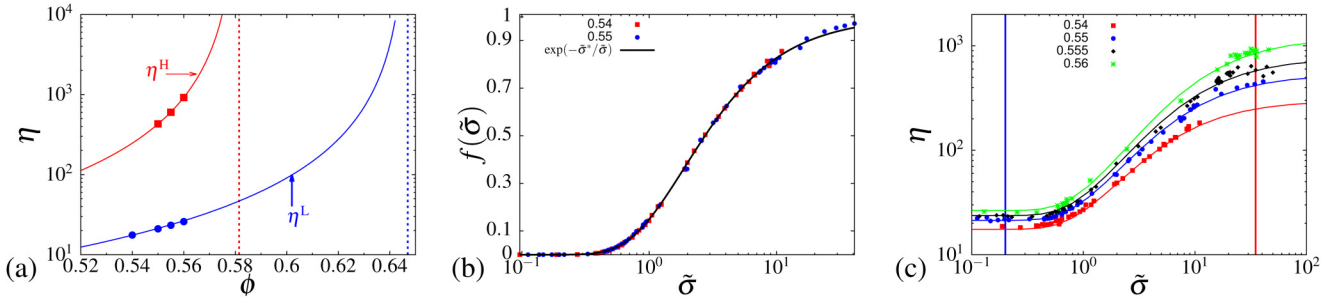

FIG. 11. (a) Rate-independent relative viscosity for low ($\tilde{\sigma} = 0.2$) and high ($\tilde{\sigma} = 35$) stresses, lines correspond to the fit. (b) The fit for the fraction of frictional contacts, $f(\tilde{\sigma})$, as a function of shear stress $\tilde{\sigma}$. (c) The fit for viscosity as a function of shear stress $\tilde{\sigma}$. Note that the friction coefficient is $\mu = 1$.

$$\frac{d\dot{\gamma}}{d\sigma} = \frac{d}{d\sigma}\left(\frac{\sigma h}{g}\right) = \frac{(\sigma h)'g - \sigma h g'}{g^2} = \frac{hg + \sigma h' g - \sigma h g'}{g^2}. \tag{A4}$$

Evaluating h' and g' gives

$$h' = 2(\phi_J^\mu - \phi_J^0)[f(\sigma)(\phi_J^\mu - \phi_J^0) + (\phi_J^0 - \phi)]\frac{df}{d\sigma}, \tag{A5}$$

$$g' = (\alpha^\mu - \alpha^0)\frac{df}{d\sigma}. \tag{A6}$$

Since the denominator g^2 of (A4) is greater than zero for all σ, $d\dot{\gamma}/d\sigma = 0$ if the numerator is zero. The numerator reduces to a differential equation in $df/d\sigma$,

$$\sigma\frac{df}{d\sigma} - \frac{[f(\sigma)(\phi_J^\mu - \phi_J^0) + (\phi_J^0 - \phi)][f(\sigma)(\alpha^\mu - \alpha^0) + \alpha^0]}{(\alpha^\mu - \alpha^0)[f(\sigma)(\phi_J^\mu - \phi_J^0) + (\phi_J^0 - \phi)] - 2(\phi_J^\mu - \phi_J^0)[f(\sigma)(\alpha^\mu - \alpha^0) + \alpha^0]} = 0. \tag{A7}$$

For $\phi < \phi_c$, no value of σ satisfies the equation. For $\phi_J^\mu > \phi > \phi_c$, there are two σ values that satisfy the equation, and for $\phi_J^0 > \phi > \phi_J^\mu$, only one σ value satisfies the equation.

The onset of DST is associated with the single fixed point at $\phi = \phi_c$, which represents the coalescence of the two fixed points found for $\phi_J^\mu > \phi > \phi_c$. The procedure for determining this single fixed point is to increment ϕ until it reaches a value $\phi_>$, identified by the fact it yields two σ values satisfying (A7). Let the last value of ϕ that does not yield such a σ value be called $\phi_<$; bisection between $\phi_<$ and $\phi_>$ can be used to determine ϕ_c and σ_c to arbitrary accuracy. Substituting the ϕ_c and σ_c values to (A1) gives $\dot{\gamma}_c$. Plotting $\chi_\sigma = \partial\sigma/\partial\dot{\gamma}$ as a function of $(\dot{\gamma} - \dot{\gamma}_c)$ reveals that near $\dot{\gamma}_c$, $\chi_\sigma \sim (\dot{\gamma} - \dot{\gamma}_c)^{-b}$ as $\dot{\gamma}_c$ is approached from either $\dot{\gamma} < \dot{\gamma}_c$ or $\dot{\gamma} > \dot{\gamma}_c$. The value of b for either direction can be determined separately by first taking the logarithm of both $(\dot{\gamma} - \dot{\gamma}_c)$ and χ_σ near the singular point, and then by calculating the slope of the line of best fit.

REFERENCES

[1] Brady, J. F., and J. F. Morris, "Microstructure of strongly sheared suspensions and its impact on rheology and diffusion," J. Fluid Mech. **348**, 103–139 (1997).

[2] Dhont, J., "On the distortion of the static structure factor of colloidal fluids in shear flow," J. Fluid Mech. **204**, 421–431 (1989).

[3] Nazockdast, E., and J. F. Morris, "Microstructural theory and the rheology of concentrated colloidal suspensions," J. Fluid Mech. **713**, 420–452 (2012).

[4] Hoffman, R., "Discontinuous and dilatant viscosity behavior in concentrated suspensions. I. Observation of a flow instability," Trans. Soc. Rheol. **16**, 155–173 (1972).

[5] Boersma, W. H., J. Laven, and H. N. Stein, "Shear thickening (dilatancy) in concentrated dispersions," AIChE J. **36**, 321–332 (1990).

[6] Cwalina, C. D., and N. J. Wagner, "Material properties of the shear-thickened state in concentrated near hard-sphere colloidal dispersions," J. Rheol. **58**, 949–967 (2014).

[7] Mari, R., R. Seto, J. F. Morris, and M. M. Denn, "Shear thickening, frictionless and frictional rheologies in non-Brownian suspensions," J. Rheol. **58**, 1693–1724 (2014).

[8] Lin, N. Y. C., B. M. Guy, M. Hermes, C. Ness, J. Sun, W. C. K. Poon, and I. Cohen, "Hydrodynamic and contact contributions to continuous shear thickening in colloidal suspensions," Phys. Rev. Lett. **115**, 228304 (2015).

[9] Boromand, A., S. Jamali, B. Grove, and J. M. Maia, "A generalized frictional and hydrodynamic model of the dynamics and structure of dense colloidal suspensions," J. Rheol. **62**, 905–918 (2018).

[10] Seto, R., R. Mari, J. F. Morris, and M. M. Denn, "Discontinuous shear thickening of frictional hard-sphere suspensions," Phys. Rev. Lett. **111**, 218301 (2013).

[11] Wyart, M., and M. E. Cates, "Discontinuous shear thickening without inertia in dense non-Brownian suspensions," Phys. Rev. Lett. **112**, 098302 (2014).

[12] Mari, R., R. Seto, J. F. Morris, and M. M. Denn, "Discontinuous shear thickening in Brownian suspensions by dynamic simulation," Proc. Natl. Acad. Sci. U.S.A. **112**, 15326–15330 (2015).

[13] Singh, A., R. Mari, M. M. Denn, and J. F. Morris, "A constitutive model for simple shear of dense frictional suspensions," J. Rheol. **62**, 457–468 (2018).

[14] Peters, I. R., S. Majumdar, and H. M. Jaeger, "Direct observation of dynamic shear jamming in dense suspensions," Nature **532**, 214–217 (2016).

[15] Yurkovetsky, Y., and J. F. Morris, "Particle pressure in sheared Brownian suspensions," J. Rheol. **52**, 141–164 (2008).

[16] Deboeuf, A., G. Gauthier, J. Martin, Y. Yurkovetsky, and J. F. Morris, "Particle pressure in a sheared suspension: A bridge from osmosis to granular dilatancy," Phys. Rev. Lett. **102**, 108301 (2009).

[17] Dong, J., and M. Trulsson, "Analog of discontinuous shear thickening flows under confining pressure," Phys. Rev. Fluids **2**, 081301 (2017).

[18] Thomas, J. E., K. Ramola, A. Singh, R. Mari, J. F. Morris, and B. Chakraborty, "Microscopic origin of frictional rheology in dense suspensions: Correlations in force space," Phys. Rev. Lett. **121**, 128002 (2018).

[19] Ódor, G., "Universality classes in nonequilibrium lattice systems," Rev. Mod. Phys. **76**, 663–724 (2004).

[20] Matsumoto, M., and S. Nakamura, "Critical exponents of nonequilibrium phase transitions in AdS/CFT correspondence," Phys. Rev. D **98**, 106027 (2018).

[21] Kussell, E., and M. Vucelja, "Non-equilibrium physics and evolution —Adaptation, extinction, and ecology: A key issues review," Rep. Prog. Phys. **77**, 102602 (2014).

[22] Morris, J. F., "Shear thickening of concentrated suspensions: Recent developments and relation to other phenomena," Annu. Rev. Fluid. Mech. **52**, 121–144 (2020).

[23] d'Haene, P., J. Mewis, and G. Fuller, "Scattering dichroism measurements of flow-induced structure of a shear thickening suspension," J. Colloid Interface Sci. **156**, 350–358 (1993).

[24] Boersma, W., P. Baets, J. Lavèn, and H. Stein, "Time-dependent behavior and wall slip in concentrated shear thickening dispersions," J. Rheol. **35**, 1093–1120 (1991).

[25] Lootens, D., H. Van Damme, and P. Hébraud, "Giant stress fluctuations at the jamming transition," Phys. Rev. Lett. **90**, 178301 (2003).

[26] Hermes, M., B. M. Guy, W. C. Poon, G. Poy, M. E. Cates, and M. Wyart, "Unsteady flow and particle migration in dense, non-Brownian suspensions," J. Rheol. **60**, 905–916 (2016).

[27] Ball, R. C., and J. R. Melrose, "Lubrication breakdown in hydrodynamic simulations of concentrated colloids," Adv. Colloid Interface Sci. **59**, 19–30 (1995).

[28] Ackerson, B. J., "Shear induced order and shear processing of model hard sphere suspensions," J. Rheol. **34**, 553–590 (1990).

[29] Seto, R., A. Singh, B. Chakraborty, M. M. Denn, and J. F. Morris, "Shear jamming and fragility in dense suspensions," Granul. Matter **21**, 82 (2019).

[30] Goldenfeld, N., *Lectures on Phase Transitions and the Renormalization Group* (CRC, Boca Raton, Florida, 2018).

[31] Melrose, J. R., and R. C. Ball, "'Contact networks' in continuously shear thickening colloids," J. Rheol. **48**, 961–978 (2004).

[32] Dorogovtsev, S. N., A. V. Goltsev, and J. F. Mendes, "Critical phenomena in complex networks," Rev. Mod. Phys. **80**, 1275–1335 (2008).

[33] Molloy, M., and B. Reed, "A critical point for random graphs with a given degree sequence," Random Struct. Algor. **6**, 161–180 (1995).

[34] Newman, M. E. J., S. H. Strogatz, and D. J. Watts, "Random graphs with arbitrary degree distributions and their applications," Phys. Rev. E **64**, 026118 (2001).